Model-based insights into the decarbonation dynamics of anion-exchange membranes

Fabian Kubannek [a], Avital Zhegur-Khais [b], Songlin Li [b], Dario R. Dekel [b,c], Ulrike Krewer [d,*]

[a] TU Braunschweig, Institute of Energy and Process Systems Engineering, Langer Kamp 19, 38106 Braunschweig, Germany
[b] The Wolfson Department of Chemical Engineering, Technion – Israel Institute of Technology, Haifa 3200003, Israel
[c] The Nancy & Stephen Grand Technion Energy Program (GTEP), Technion - Israel Institute of Technology, Haifa 3200003, Israel
[d] Karlsruhe Institute of Technology, Institute for Applied Materials – Electrochemical Technologies, Adenauerring 20b, 76131 Karlsruhe, Germany

ARTICLE INFO

Keywords:
Fuel cells
Hydroxide conductivity
Modelling and simulation
Diffusivity
Migration

ABSTRACT

We present a model-based analysis of the transport of anions in anion exchange membranes (AEMs) with the aim of understanding the decarbonation process and its dynamics. The dynamic simulation model covers the diffusive and migrative transport of water, carbonate anions, and hydroxide anions through an AEM. To the best of our knowledge, this is the first model studying decarbonation process in AEMs. The model is validated using decarbonation data from anion conductivity measurements of ten different AEM materials. Driven by migrative transport, strong concentration gradients develop inside the membranes. A parameter study reveals that the ion-exchange capacity and the applied current have the largest effect on the decarbonation dynamics. Further, high hydroxide diffusivities increase the decarbonation time constant, whereas high carbonate diffusivities decrease it. The results further indicate that high diffusivities of both carbonates and hydroxide result in slower membrane decarbonation. This work provides new insights into properties determining the carbonation and decarbonation of AEMs, which is critical for AEM-based electrochemical devices such as fuel cells and electrolysers.

1. Introduction

Anion-exchange membrane fuel cells (AEMFCs) are promising energy converter devices because, in the alkaline environment of the anion exchange membrane (AEM), low-cost materials can be employed [1–9]. Significant advances in AEMFC research bring this technology closer to real applications. Having said that, some remaining challenges still need to be overcome, among them, AEM alkaline stability and carbonation issues [10]. Unless new highly efficient CO_2 sequestration techniques are developed [11], carbonation processes occur during the operation of AEMFCs under ambient air containing CO_2 [12].

When AEMFCs operate with ambient air, hydroxide ions generated from the oxygen reduction reaction on the cathode side react with CO_2 and form carbonates (see eq. (1) and (2)).

$$OH^- + CO_2 \leftrightarrow^{r_{c1}} HCO_3^- \tag{1}$$

$$HCO_3^- + OH^- \leftrightarrow^{r_{c2}} CO_3^{2-} + H_2O \tag{2}$$

The equilibrium reactions result in a nearly complete exchange of hydroxide ions to bicarbonate and carbonate ions when the membrane is in contact with air [13,14].

Using solid alkaline electrolytes like AEM prevents the precipitation of carbonates that is observed in liquid alkaline systems [15,16]. However, all CO_2-exposed alkaline systems still suffer from the adverse effects of carbonate species [17,18]. The lower ion mobility of carbonates compared to hydroxide reduces the ionic conductivity in the membrane and the ionomer. Furthermore, the reaction overpotential at the anode and its open circuit potential increase with a pH decrease. The effects significantly reduce the overall fuel cell performance [19–21]. It has been reported that AEMs in a carbonated state are chemically more stable than membranes in a hydroxide state because carbonates are not as nucleophilic as hydroxide anions [22]. On the other hand, it has also been shown that (bi)carbonate ions reduced the water solvation of the hydroxides, increasing then the possibility of a faster degradation of the AEM [23]. Understanding and decreasing the negative effect of CO_2 on the AEMs and the electrodes is an open challenge of utmost importance for AEMFC commercialization, as operation with ambient air is the only attractive and practical option for most applications.

Research interest in this area has been increasing recently with experimental investigations of AEMFC performance under the influence

* Corresponding author.
E-mail address: ulrike.krewer@kit.edu (U. Krewer).

of CO_2 [21,24], ex-situ measurements of the membrane decarbonation [25–27], and simulations of the cell behavior under the influence of CO_2 [20,28]. These studies show, on one hand, that the addition of CO_2 to an AEMFC has a severe negative impact due to the AEM carbonation, where the cell operating voltage is generally decreased by 200–400 mV depending on the reaction conditions. On the other hand, these studies prove that decarbonation can occur while applying current to the AEM. However, there are no models describing this decarbonation phenomenon. Nevertheless, the influence of CO_2 on the AEMs is not yet fully understood. Especially the decarbonation dynamics and the corresponding development of ion concentration profiles over time in the membranes are addressed in only a few studies. Understanding the dynamics is important, as it allows one to assess and optimize the startup or dynamic operation of the fuel cell.

Dynamic AEM studies include simulation studies by Myles et al. [29], who simulated the carbonation process of two different AEMs when exposed to air but in the absence of current, and work by Wrubel et al. [30], who simulated the decarbonation dynamics of an AEMFC cell focusing on the mechanism of the CO_2 release at the anode. Recent experimental work has been reported by Zhegur-Khais et al. [25], who experimentally studied the decarbonation of different AEM in a setup to determine the true hydroxide conductivity of the membranes. Similarly, Cao et al. [31] experimentally investigated the decarbonation of AEM with a pH indicator in a similar setting, which enabled the visualization of concentration fronts moving through the AEM.

When an AEMFC is operated at a high current density, the carbonate concentration in the membrane is strongly reduced because carbonates are diluted by the high rate of hydroxide production at the cathode, from where the ions are driven to the anode by migration [28]. This process is also referred to as self-purging mechanism. During self-purging, a local carbonate accumulation occurs at the anode, and back-diffusion of carbonates is induced. Therefore, it is crucial to understand the transport of carbonates and the interplay of migration and diffusion under conditions when an ionic current is flowing through the membrane. A thorough understanding of parameters and processes that determine the decarbonation process and its dynamics will facilitate the development of AEMs for improved AEMFCs for an efficient operation with ambient air under dynamic load profiles and during startup.

In this work, we present a dynamic model that describes the *ex-situ* decarbonation of AEMs and analyze the effect of various parameters on the electrochemical de-carbonation process. The model is validated using decarbonation data from ten commercially available and research AEMs reported by Zhegur-Khais et al. [25]. The simulation results reveal deeper insights into transport and concentration gradients inside the membranes under relevant conditions. Finally, the factors influencing the velocity of the decarbonation process are discussed in detail. This work contributes to a better understanding of the AEM decarbonation process and the behavior of AEM in AEMFCs operated with ambient air.

2. Experimental

Conductivity measurements during decarbonation - A large set of experimental data for model validation is taken from the literature [25]. The data were recorded by a recent ex-situ decarbonation method developed by Dekel's group [25,26]. In brief, a membrane in carbonate form is placed in a four-electrode conductivity measurement cell under a nitrogen flow with controlled humidity and temperature. After an equilibration time of approximately-three hours, a direct current is applied between the two outer electrodes. Water is split at the electrodes, and hydroxide anions are produced at the cathode electrode. The generated hydroxide anions replace the carbonates resulting in an in-situ exchange of the AEM to its fully OH^- form. To observe the ion exchange from carbonate to hydroxide, the variation of ionic conductivity, which results from the difference in ion mobility of hydroxides and carbonates, is recorded over time using two sensing electrodes. These decarbonation experiments allow us to study the ion transport processes with an applied external current under controlled conditions. A detailed description of the setup can be found in [26], and the experimental data are discussed in [25].

The AEMs investigated in [25] include Tokuyama A201 (Tokuyama Corporation, Japan); Sustainion® RT and Sustainion® Grade 60 (Dioxide Materials, USA), named hereafter Sustainion RT and Sustainion 60, respectively; AT-1 (Hespas-Energy, China); FAA-3 (FuMaTech, Germany); ETFE-TMA and LDPE-BTMA [32,33] developed and supplied by Prof. Varcoe (Surrey University, UK); PF-AEM [34] obtained from Dr. Pivovar (National Renewable Energy Laboratory, CO, USA), named hereafter PF; PAPip membrane[35] obtained from Prof. Jannasch (Lund University, Sweden); and QPAF-4(TM) [36] obtained from Prof. Miyatake (Yamanashi University, Japan).

The values of the membrane-specific properties IEC, water uptake, and membrane geometry are based on data reported in [25] and can be found in Table 1, in addition to further parameters. The current density for the different membranes is calculated for a constant current of 0.1 mA, which was applied in all experiments, unless noted otherwise. Due to different cross-sectional areas, the current density differs among the membranes.

Visualization of the decarbonation process - Additional tests to visualize the decarbonation process were carried out in this study. An anion exchange membrane (low-density polyethylene functionalized with benzyl trimethylamine [32,37], LDPE-BTMA, developed and supplied by Prof. Varcoe from Surrey University, UK) was immersed in thymolphthalein solution (0.2 wt% in 1:2 ethanol:water solution) for 24 h, followed by immersion in 1 M $KHCO_3$ aqueous solution for 24 h, to convert the AEM into its bicarbonate form. Finally, the AEM was rinsed in ultrapure water for 24 h to remove the excess electrolyte. This procedure was repeated every time before a new test was carried out. The membrane was then placed in an MTS740 four-electrode cell head (Scribner Associates). A constant current was then applied across the membrane by an Ivium-*n*-Stat (Ivium Technologies) under 100 sccm/min nitrogen flow. Water was added regularly during the experiment to keep the membrane in a fully humidified state. As hydroxide ions start flowing, the local pH increases until the absorbed thymolphthalein changes color from white to a bluish color. Pictures were taken every 10 min to record the dynamics of the decarbonation process. The tests were repeated at three levels of current values (0.1, 0.3, and 0.5 mA) to compare results with the developed model.

3. Modeling

We adapted and extended a previously developed AEMFC model [28] to describe the dynamic changes in conductivity and ion concentration of the membranes during the decarbonation processes. The model describes the effect of carbonation on the AEMFC under steady-state conditions. Full details of the model are given elsewhere [28]. In this section, the adapted model structure and the equations are explained.

Fig. 1 shows the model structure and the processes considered in the adapted model developed in this study. Initially, at $t = 0$, the membrane is in a full carbonate state, and no CO_2 is present in the gas phase. When the constant current operation is started, the hydrogen evolution reaction (HER) takes place at the cathode, producing hydroxide ions onto the AEM. Hydroxide and carbonate ions are transported towards the anode electrode, where the oxygen evolution reaction (OER) takes place, and carbonates are converted to and released as CO_2 gas. The nitrogen flow over the membrane surface leads to a diffusive boundary layer. In the membrane, CO_2 is formed from carbonates; it can change to the gas phase at the interface between the membrane and the boundary layer.

In the following, the modeled processes and governing equations for all domains of the model will be detailed.

Membrane - The key processes for the exchange of anions in the membrane during the conductivity measurement are the transport of ions through the membrane and the reactions between carbonate and

Table 1
Properties of various evaluated AEMs as reported in [25] and resulting current density.

Membrane	IEC (mmol/g)	$f_W^{M,eq}$(%)	Density ρ_{dry}^{M} (g cm^{-3})	Width w^M (cm)	Thick-ness d^M (μm)	Cross-section area[+] A^c (cm^2)*10^3	Current density i (mA cm^{-2})
A201	1.58	38.2	0.94	1.02	32.8	3.3	29.9
FAA-3	1.43	26.2	0.99	0.75	33.8	2.5	39.4
Sustanion RT	1.47	52.3	0.90	1.40	69.6	10	9.7
Sustanion 60	1.44	50.6	0.80	1.29	79.6	9.7	10.3
ETFE-TMA	1.59	43.5	1.10	0.96	44.2	4.2	23.6
AT-1	2.12	30.4	1.02	1.25	59.2	7.4	13.5
PF	0.92	25.9	1.07	1.11	48.6	5.4	18.5
LDPE-BTMA	2.39	74.8	0.87	1.10	59.0	6.5	15.4
PAPip	1.85	37.4	1.00	1.19	56.0	6.7	15.0
QPAF-4(TM)	1.07	26.4	0.99	1.00	28.0	2.8	35.7

[+] In the experimental setup, conductivity was measured in-plane and the cross-sectional area for the current flow is thus $A^c = w^M * d^M$.

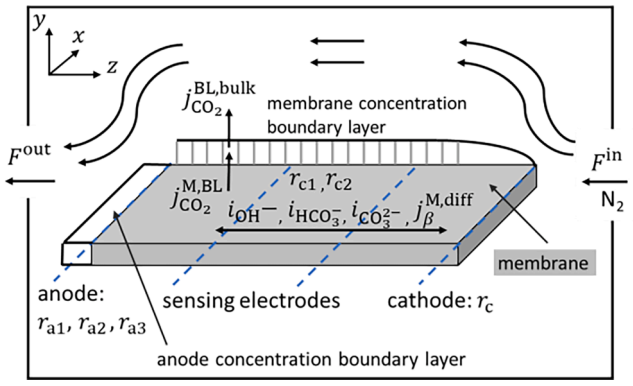

Fig. 1. Schematic illustration of the modeling domain and the processes considered in the model. A constant current is applied between anode and cathode. At the cathode, hydroxide ions are formed (r_c), which gradually replace the carbonates in the membrane. Migration (i_{ion}) and diffusion ($j_\beta^{M,diff}$) govern the transport of ions through the membrane. At the anode, hydroxide and (bi)carbonate anions are oxidized electrochemically (r_{a1}, r_{a2}, r_{a3}), A constant stream of nitrogen F^{in} enters the setup. At the membrane/gas interfaces, gaseous CO_2 is released to a concentration boundary layer $\left(j_{CO_2}^{M,BL}\right)$ from where it enters the gas bulk volume $j_{CO_2}^{BL,bulk}$ and leaves the cell with the gas flow F^{out}.

hydroxide ions. Ions are transported through the membrane by migration and diffusion. The hydroxide ions react with carbon dioxide and bicarbonate according to Eq. (1) and (2) to form bicarbonate and carbonate. These reactions are not very fast and do not quickly reach equilibrium [29]. The corresponding rates of the chemical carbonation reactions in the AEM, r_{c1} for eq. (1) and r_{c2} for eq. (2), are described by finite reaction rates for reversible reactions:

$$r_{c1} = k_{c1f} a_{CO_2^{aq}} a_{OH^-} - k_{c1b} a_{HCO_3^-} \tag{3}$$

$$r_{c2} = k_{c2f} a_{HCO_3^-} a_{OH^-} - k_{c2b} a_{H_2O} a_{CO_3^{2-}} \tag{4}$$

where a_i are the activities of the species (OH^-, CO_3^{2-}, HCO_3^-), and k_i are the forward and backward reaction rate constants. The calculation of corresponding activity coefficients is conducted with the Truesdell-Jones model as described elsewhere [28].

In AEM, the dissociation of anions from the cationic groups e attached to the membrane backbone is not complete [28]. Thus, only the free anions in the membrane are available for reactions and transport. The activities of species participating in the chemical reactions and the concentration gradients in the membrane are based on the concentrations of the free ions. Since the pK_B values of the cationic groups and factors influencing the dissociation are unknown, the dissociation is not modeled in detail here. Instead, the free ion concentrations in the membrane, $\tilde{c}_{ion}^{M}$, are linked to the concentration of the respective ion in the membrane c_{ion}^{M} assuming a constant dissociation factor α_{ion}^{diss}, similar to what was reported in [28] (see SI1 for further details):

$$\tilde{c}_{ion}^{M} = \alpha_{ion}^{diss} c_{ion}^{M} \tag{5}$$

To model the transport and concentration changes in the membrane, the membrane is spatially discretized in the direction of the ionic current (z-direction in Fig. 1) because large concentration gradients occur in this direction. Transport in x-direction is neglected because of negligible concentration gradients in x-direction, as only very little CO_2 will evaporate through the small interface plane y-z. Transport in the through-plane direction (y-direction in Fig. 1) is considered because dissolved CO_2 can leave the membrane at the large membrane surface (x-z plane) and change to the gas phase. However, no gradients are spatially resolved in this direction because the length of the membrane is much larger than its thickness. The species balance, including the transport through the membrane, is described by the following balance equations:

$$\frac{\partial c_{OH^-}^{M}}{\partial t} = -\frac{\partial j_{OH^-}^{M}}{\partial z} + \frac{1}{F}\frac{\partial i_{OH^-}^{mig}}{\partial z} - r_{c1} - r_{c2} \tag{6}$$

$$\frac{\partial c_{HCO_3^-}^{M}}{\partial t} = -\frac{\partial j_{HCO_3^-}^{M}}{\partial z} + \frac{1}{F}\frac{\partial i_{HCO_3^-}^{mig}}{\partial z} + r_{c1} - r_{c2} \tag{7}$$

$$\frac{\partial c_{CO_3^{2-}}^{M}}{\partial t} = -\frac{\partial j_{CO_3^{2-}}^{M}}{\partial z} + \frac{1}{2F}\frac{\partial i_{CO_3^{2-}}^{mig}}{\partial z} + r_{c2} \tag{8}$$

$$\frac{\partial c_{CO_2^{aq}}^{M}}{\partial t} = -\frac{\partial j_{CO_2^{aq}}^{M}}{\partial z} - \frac{j_{CO_2}^{M,BL}(z)}{d^M} - r_{c1} \tag{9}$$

with the concentrations of the species in the membrane c_β^M, the thickness of the membrane d^M, the diffusive fluxes within the membrane j_β^M, the flux of CO_2 leaving the membrane into the gas phase $j_{CO_2}^{M,BL}$, and the partial current densities i_{ion}^{mig} for the charge transport by migration defined by:

$$i_{ion}^{mig} = -\sigma_{ion}\frac{\partial \Phi}{\partial z} \tag{10}$$

where σ_{ion} is the ionic conductivity and Φ is the electric potential in the membrane. The total ionic conductivity at any point in the membrane is the sum of the individual conductivities of hydroxide, bicarbonate, and carbonate ions.

$$\sigma^M = \sum_{ion}\sigma_{ion} \tag{11}$$

Ionic conductivities are calculated by [28]:

$$\sigma_{ion} = \left(\varepsilon^M\right)^{1.5}\frac{F^2}{RT}\frac{(z_{ion})^2 \tilde{c}_{ion}^{M} D_{ion}^{M}}{x_W^M(1+\delta_{ion})} \tag{12}$$

With the membrane porosity $\varepsilon^{M} = \frac{f_W^M \rho_{dry}^M}{\rho_{Wl}}$, the mole fraction of water in the membrane $x_W^M = \frac{f_W^M}{f_W^M + M_W IEC}$, and the diffusivity ratio δ_{ion}. f_W^M is the membrane water uptake. ρ_{dry}^M is the density of the dry membrane, ρ_{Wl} is the density of liquid water, M_W is the molar weight of water, R is the universal gas constant, T is the temperature, and IEC is the ion exchange capacity of the membrane. The diffusivity ratio δ_{ion} is calculated by [28]:

$$\delta_{ion} = \frac{M_W\, IEC}{f_W^M}\left(\frac{\rho_{Wl}}{M_W\, IEC\, \rho_{dry}^M}\right)^{2/3}\left(1 + \frac{M_{ion}}{M_W}\right)^{1/2} \tag{13}$$

The overall current density corresponds to the sum of all charge transport processes.

$$i = \sum_{ion}(i_{ion}^{mig} + z_{ion} F j_{ion}^M) \tag{14}$$

The concentrations of dissolved CO_2 and the anion species are low. Therefore the diffusive fluxes j_β^M of dissolved species $\beta \in \{CO_2^{aq}, OH^-, CO_3^{2-}, HCO_3^-\}$ are calculated by Fick's law of diffusion:

$$j_\beta^M = -D_\beta^M (\varepsilon^M)^{1.5} \frac{\partial c_\beta^M}{\partial z} \tag{15}$$

Studies conducted on our prior model [16] showed that water uptake is constant everywhere for the experimental setup used to generate the experimental data. Because of the large interface between the membrane and the gas phase, water is in equilibrium with the water vapor from the gas phase everywhere. Thus, water transport and gradients in membrane water uptake are not considered. Inaba et al. also confirmed in their simulations [9] that water transport in z-direction is negligible. The membrane water uptake f_W^M was set equal to the experimentally measured water uptake $f_W^{M,\,eq}$. Furthermore, it is assumed that phase changes at the interface of the boundary layer and membrane are fast so that the activity of dissolved CO_2 in the membrane, $a_{CO_2^{aq}}^{M,MBL}$, is in equilibrium with the partial pressure of gaseous CO_2 $p_{CO_2}^{MBL}$ and the corresponding gas phase concentration $c_{CO_2}^{M,MBL}$ at the interface:

$$a_{CO_2^{aq}}^{M,MBL} = K_{CO_2} p_{CO_2}^{MBL} = K_{CO_2} c_{CO_2}^{M,MBL} RT \tag{16}$$

K_{CO_2} is the activity-based Henry constant. It has been shown by Myles et al. [29] that a phase equilibrium at the interface is a justified assumption for a membrane in the absence of current, and their finding also holds for a membrane through which an ionic current is flowing. The diffusive transport over the phase boundary is described by the following diffusion equation for the gaseous phase:

$$j_{CO_2}^{M,MBL} = 2D_{CO_2} \frac{c_{CO_2}^{M,MBL} - c_{CO_2}^{MBL}}{0.5 d^{BL}} \tag{17}$$

With the gaseous binary diffusion coefficient for CO_2 in nitrogen D_{CO_2}. $c_{CO_2}^{MBL}$ is the concentration in the middle of the boundary layer of thickness d^{BL}. $c_{CO_2}^{M,MBL}$ is the concentration at the interface (for details, see boundary layer model below). Factor 2 is added because transport occurs through the upper and lower surface of the membrane. The transport over the phase boundary must also equal the transport from the center of the membrane to the interface.

$$j_{CO_2}^{M,MBL} = 2D_{CO_2}^M \frac{c_{CO_2}^M - c_{CO_2^{aq}}^{M,BL}}{0.5 d^M} \tag{18}$$

Combining eq. (16) – (18), the concentrations at the interface and the transport terms can be calculated.

Cathode - At the cathode, hydroxide ions are produced onto the membrane according to:

$$H_2O + e^- \xrightarrow{r_c} OH^- + \frac{1}{2} H_2 \tag{19}$$

Thus, r_c is directly proportional to the total current I: $r_c = \frac{I}{F}$.

The cathode is modeled as a phase boundary without volume. This is a simplification justified by the fact that the model's purpose is to describe the membrane processes. All produced hydroxide ions are transported into the membrane by migrative transport, which is directly proportional to the applied current. No other ions enter the membrane from the cathode:

$$i_{OH^-}^{mig}(z = l) = -I \tag{20}$$

$$i_{CO_3^{2-}}^{mig}(z = l) = 0 \tag{21}$$

$$i_{HCO_3^-}^{mig}(z = l) = 0 \tag{22}$$

An equilibrium between gaseous CO_2 in the boundary layer and dissolved CO_2 is assumed at the interface between the cathode and the boundary layer, similar to the membrane.

Anode - At the anode, the oxygen evolution reaction takes place via reactions (23)-(25):

$$OH^- \xrightarrow{r_{a1}} \frac{1}{2} H_2O + \frac{1}{4} O_2 + e^- \tag{23}$$

$$HCO_3^- \xrightarrow{r_{a2}} \frac{1}{2} H_2O + \frac{1}{4} O_2 + CO_2 + e^- \tag{24}$$

$$CO_3^{2-} \xrightarrow{r_{a3}} \frac{1}{2} O_2 + CO_2 + 2e^- \tag{25}$$

As discussed in our previous modeling work [28], the reaction mechanism at the anode does not need to be resolved in detail to obtain an accurate mass balance. All anions that reach the anode are consumed in an electrochemical reaction that may either be the direct conversion of carbonates to oxygen and CO_2 or a reaction of carbonates with water to form hydroxide ions, directly followed by the electrochemical oxidation of hydroxide to oxygen.

The reaction rates are described by:

$$r_{a1} = \frac{A^c}{zF} i_{OH^-}^{mig}\Big|_{z=0} \tag{26}$$

$$r_{a2} = \frac{A^c}{zF} i_{HCO_3^-}^{mig}\Big|_{z=0} \tag{27}$$

$$r_{a3} = \frac{A^c}{zF} i_{CO_3^{2-}}^{mig}\Big|_{z=0} \tag{28}$$

where A^c is the cross-sectional area of the membrane. CO_2 is removed by a diffusive flow between the anode and the anode concentration boundary layer $\dot{n}_{CO_2}^{A,ABL}$ and by a diffusive flow into the membrane $\dot{n}_{CO_2^{aq}}^{MA}$. Since the anode is also described as a phase boundary without volume, the following steady-state balance equation for CO_2 at the anode results:

$$0 = \dot{n}_{CO_2^{aq}}^{M,A} + r_{a2} + r_{a3} - \dot{n}_{CO_2}^{A,ABL} \tag{29}$$

$\dot{n}_{CO_2}^{A,ABL}$ is the transport of gaseous CO_2 from the anode into the boundary layer, given by:

$$\dot{n}_{CO_2}^{A,ABL} = A^c D_{CO_2} \frac{c_{CO_2}^A - c_{CO_2}^{ABL}}{0.5 d^{BL}} \tag{30}$$

where $c_{CO_2}^{ABL}$ is the concentration in the middle of the anode boundary layer (see below). An equilibrium between gaseous CO_2 and dissolved CO_2 is assumed at the interface between the anode and boundary layer similar to the membrane.

$\dot{n}_{CO_2^{aq}}^{M,A}$ is the transport of dissolved CO_2 from the membrane to the anode:

$$\dot{n}^{\mathrm{M,A}}_{\mathrm{CO_2^{aq}}} M,A = A^{c} D^{\mathrm{M}}_{\mathrm{CO_2}} \left.\frac{\partial \tilde{c}^{\mathrm{M}}_{\mathrm{CO_2}}}{\partial z}\right|_{z=0} \tag{31}$$

Boundary layer - The thickness of the diffusion boundary layer around the membrane, d^{BL}, is calculated by the following equations assuming a laminar flow over a flat plate:

$$d^{\mathrm{BL}} = \frac{\delta^{\mathrm{hydro}}}{Sc} \tag{32}$$

$$Sc = \frac{\nu}{D_{\mathrm{CO_2}}} \tag{33}$$

$$\delta^{\mathrm{hydro}} = 4.91\sqrt{\frac{\nu l^{\mathrm{M}}}{2u_0}} \tag{34}$$

with the Schmidt number Sc, the kinematic viscosity of air ν, the thickness of the hydrodynamic boundary layer δ^{hydro}, the length of the membrane in the flow direction l^{M}, and the free flow velocity of the gas u_0. Since the free flow velocity is approximately 0.005 m s^{-1} and the Reynolds number thus far below 100, laminar flow can be assumed. Inside the boundary layer, only a balance equation for CO_2 is established because the production of oxygen and hydrogen is negligible compared to the nitrogen flow rate.

The boundary layer is divided into the anode boundary layer and the membrane boundary layer. Both parts of the boundary layer are described as ideally mixed volumes with the averaged concentrations c^{ABL} and c^{BL}. The corresponding species balances are given by the following ordinary differential equations:

$$\frac{\mathrm{d}c^{\mathrm{BL}}_{\mathrm{CO_2}}}{\mathrm{d}t} V^{\mathrm{BL}} = \dot{n}^{\mathrm{M,MBL}}_{\mathrm{CO_2}} - \dot{n}^{\mathrm{BL,bulk}}_{\mathrm{CO_2}} \tag{35}$$

$$\frac{\mathrm{d}c^{\mathrm{ABL}}_{\mathrm{CO_2}}}{\mathrm{d}t} V^{\mathrm{ABL}} = \dot{n}^{\mathrm{A,ABL}}_{\mathrm{CO_2}} - \dot{n}^{\mathrm{ABL,bulk}}_{\mathrm{CO_2}} \tag{36}$$

with the volume of the membrane and anode boundary layer $V^{\mathrm{MBL}} = A^{s} d^{\mathrm{BL}}$ and $V^{\mathrm{ABL}} = A^{c} d^{\mathrm{BL}}$. The membrane surface area $A^{s} = 2l^{\mathrm{M}} w^{\mathrm{M}}$ is twice as big as the product of the length l^{M} and width w^{M} of the membrane because the top and bottom sides of the membrane are added up.

The transport between the membrane and the membrane boundary layer is defined by:

$$\dot{n}^{\mathrm{M,MBL}}_{\mathrm{CO_2}} = D_{\mathrm{CO_2}} \int_{z=0}^{z=l^{\mathrm{M}}} 2w^{\mathrm{M}} \frac{c^{\mathrm{M,MBL}}_{\mathrm{CO_2}} - c^{\mathrm{MBL}}_{\mathrm{CO_2}}}{0.5 d^{\mathrm{BL}}} \mathrm{d}z \tag{37}$$

The transport of CO_2 between the boundary layers and the bulk volume of the test cell is defined by:

$$\dot{n}^{\mathrm{MBL,bulk}}_{\mathrm{CO_2}} = D_{\mathrm{CO_2}} A^{s} \frac{c^{\mathrm{MBL}}_{\mathrm{CO_2}} - c^{\mathrm{bulk}}_{\mathrm{CO_2}}}{0.5 d^{\mathrm{BL}}} \tag{38}$$

$$\dot{n}^{\mathrm{ABL,bulk}}_{\mathrm{CO_2}} = D_{\mathrm{CO_2}} A^{c} \frac{c^{\mathrm{ABL}}_{\mathrm{CO_2}} - c^{\mathrm{bulk}}_{\mathrm{CO_2}}}{0.5 d^{\mathrm{BL}}} \tag{39}$$

Gas bulk volume – The change in CO_2 concentration in the gas bulk volume $c^{\mathrm{bulk}}_{\mathrm{CO_2}}$ is described by the following equation, assuming a well-mixed bulk chamber:

$$\frac{\mathrm{d}c^{\mathrm{bulk}}_{\mathrm{CO_2}}}{\mathrm{d}t} V^{\mathrm{bulk}} = \dot{n}^{\mathrm{MBL,bulk}}_{\mathrm{CO_2}} + \dot{n}^{\mathrm{ABL,bulk}}_{\mathrm{CO_2}} - F c^{\mathrm{bulk}}_{\mathrm{CO_2}} \tag{40}$$

with the cell volume V^{bulk} and the volumetric flow rate F.

It is still subject to debate which ion is dominant in the carbonated AEM, bicarbonate [38,39] or carbonate [40]. In the initial state of the model, the CO_2 concentration in the gas phase is zero (100 % nitrogen), and the concentrations of OH^-, CO_3^{2-} and HCO_3^{2-} equal the equilibrium values that result in a membrane in contact with air containing 400 ppm CO_2. Simulations with different initial conditions (see fig. SI2) showed that the model is not very sensitive to the initial conditions because bicarbonate is quickly converted to carbonate in a CO_2-free environment, regardless of the initial ratio of carbonate and bicarbonate. The selected initial conditions were chosen to improve numerical stability by starting in a situation where the concentrations of the ionic species are near their equilibrium values.

Partial differential equations were discretized using a finite volume scheme. The model was implemented in MATLAB and solved by the ode15s solver.

The only adjustable model parameters are the diffusion coefficients of the ionic species $D^{\mathrm{M}}_{\mathrm{ion}}$. They will be discussed in the results section. Fixed model parameters and their values are summarized in Table 2.

4. Results and discussion

The model is used to reveal the transport and reaction processes and their interaction during the decarbonation of the various AEMs. The factors that affect the dynamics of the decarbonation are investigated to identify which membrane properties promote or impede the removal of carbonates from AEM.

The model is validated by comparing simulation results to the measurements of anion conductivity during the decarbonation process from Zhegur-Khais et al. [25]. In the experiments, the conductivity was measured by two sensing electrodes placed in the middle of the membrane with a 4 mm distance between them. For a direct comparison between experimental and simulation, the simulated conductivity is evaluated in the same interval. It is calculated by:

$$\sigma^{\mathrm{M,\,middle}} = \frac{1}{R^{\mathrm{M,middle}}} = \frac{1}{\int_{z=7\mathrm{mm}}^{z=13\mathrm{mm}} \frac{\mathrm{d}z}{\sigma^{\mathrm{M}}}} \tag{41}$$

4.1. A case study of a fast vs A slowly decarbonating membrane

In this section, a membrane that is decarbonated quickly and a membrane that is de-carbonated slowly are analyzed and compared in order to elucidate the factors that determine the decarbonation dynamics.

The LDPE-BTMA membrane decarbonates comparatively slowly. The values of the ion diffusivities for the simulation of the LDPE-BTMA membrane ($D^{\mathrm{M}}_{\mathrm{OH^-}}$=1.5 10^{-8} m^2/s $D^{\mathrm{M}}_{\mathrm{CO_3^{2-}}}$ = 2.3 10^{-9} m^2/s $D^{\mathrm{M}}_{\mathrm{HCO_3^-}}$ = 4.5 10^{-9} m^2/s) were identified by manually adjusting the diffusivities until an agreement of experiment and simulation was reached. $D^{\mathrm{M}}_{\mathrm{OH^-}}$ was adjusted to reach the experimental conductivity at the end of the experiment when the membrane was in hydroxide form. $D^{\mathrm{M}}_{\mathrm{CO_3^{2-}}}$ was

Table 2
Model parameters.

Parameter	Value	Parameter	Value
u_0	5.2×10^{-3} m/s	$\alpha^{\mathrm{diss}}_{\mathrm{CO_3^{2-}}}$	0.2 [see SI]
l^{M}	20×10^{-2} m	T	313.15 K
ν	1.57×10^{-5} m^2/s [41]	k_{c1f}	8.75×10^{6} $kg^2\,mol^{-1}\,m^{-3}\,s^{-1}$ [28]
F	8.3 mL s^{-1}	k_{c1b}	0.53 kg m^{-3} s^{-1} [28]
V^{bulk}	0.25 L	k_{c2f}	8.75×10^{7} $kg^2\,mol^{-1}\,m^{-3}\,s^{-1}$ [28]
RH^{in}	95 %	k_{c2b}	4.32×10^{4} $kg^2\,mol^{-1}\,m^{-3}\,s^{-1}$ [28]
p^{in}	1 bar	$a_{\mathrm{H_2O}}$	1 mol kg^{-1} [28]
ρ_{wl}	991.9 kg m^{-3}	$K_{\mathrm{CO_2}}$	0.025 mol kg^{-1} atm^{-1} [28]
$z_{\mathrm{OH^-}}$	−1	$D^{\mathrm{M}}_{\mathrm{ion}}$	See results section
$z_{\mathrm{CO_3^{2-}}}$	−2	$D^{\mathrm{M}}_{\mathrm{CO_2}}$	2.87×10^{-9} m^2/s [28]
$z_{\mathrm{HCO_3^-}}$	−1	$D_{\mathrm{CO_2}}$	1.77×10^{-5} m^2/s [28]
$\alpha^{\mathrm{diss}}_{\mathrm{OH^-}}$	0.4 [see SI]		
$\alpha^{\mathrm{diss}}_{\mathrm{HCO_3^-}}$	0.4 [see SI]		

adjusted to reach the experimental conductivity at the beginning of the experiment when the membrane was in carbonate form. $D^{M}_{HCO_3^-}$ was set to 200 % of $D^{M}_{CO_3^{2-}}$.

Fig. 2 a) shows the simulated and measured anion conductivity values of the LDPE-BTMA membrane over time for a current of 0.1 mA. Initially, the membrane is fully carbonated, and the conductivity is low. After an equilibration period of 4 h, a current of 0.1 mA is applied, which produces OH^- ions at the cathode via *in-situ* water electrolysis. The OH^- and carbonate ions migrate through the AEM to the anode, where the carbonates are released in the form of CO_2 [26]. Due to this process, the anion conductivity continuously increases. After approximately 50 h, all carbonates are exchanged, and the membrane reaches the fully OH^- form. The LDPE-BTMA membrane is decarbonated comparatively slowly among the membranes investigated in [25]. The simulated and experimental conductivities agree very well.

In Fig. 2 b), the simulated hydroxide ion concentration is shown for every location in the membrane and for the entire decarbonation process. Once the current is switched on, carbonate is replaced by hydroxide ions, beginning at the cathode side, where hydroxide is generated by the HER. It can be seen that strong concentration gradients are developed in the membrane during the decarbonation process. The cathode side reached a hydroxide concentration of 1 mol/L 22 min after the current was applied. At the same time, the hydroxide concentration at the anode side is only 3.5 mmol/L, ca. three orders of magnitude lower. The hydroxide ions move through the membrane as a concentration front which broadens over time while moving from cathode to anode. The reason for this broadening of the concentration front is diffusion which flattens the concentration gradients.

In Fig. 2 c), the evolution of the anion concentrations over time is shown at three selected locations: at the anode side, the cathode side, and in the middle of the membrane. The initial bicarbonate concentration drops during equilibration before the current is switched on. The negligible amount of bicarbonate in AEM is consistent with the findings in our previous studies of AEMFC operated under CO_2-containing (ambient) air [28]. The membrane is almost entirely in a carbonate state after 4 h. However, the carbonate concentration rapidly decreases under the current operation. At 50 h, the carbonate concentrations all over the membrane have fallen to almost zero. The decarbonation is thus completed, and the membrane is in its full OH^- form.

The hydroxide concentration front moving from cathode to anode was further verified by observing the decarbonation of an LDPE-BTMA membrane, to which a pH indicator had been added to make the increase in OH^- concentration visible. In Fig. 3, the experimental pictures showing the moving color front in a membrane treated with an indicator solution and the simulated hydroxide ion concentration fronts as comparison are shown. As can be seen, as the current is increased, the decarbonation dynamics increase, and the exchange to hydroxide ions occurs more rapidly towards the anode side. At all current values, an excellent agreement between both experimental and simulated dynamics of the decarbonation can be seen by comparing Fig. 3a and 3b. These results validate the model developed in this study, increasing the strength of the findings.

Next, the processes that cause the observed dynamics and govern the decarbonation process are elucidated. In Fig. 4 a), the rates of migrative and diffusive transport in the middle of the membrane are shown over time for OH^- and CO_3^{2-}. During the decarbonation process, transport by migration is much larger than transport by diffusion for both OH^- and CO_3^{2-}. For instance, at 5 h, one hour after the current has been applied, the rate of migrative transport of OH^- is 0.16 nmol s^{-1}, whereas the rate of diffusive transport is 0.04 nmol s^{-1}. The rate of migrative transport of CO_3^{2-} is 0.41 nmol s^{-1}, whereas the rate of diffusive transport is − 0.003 nmol s^{-1}. Migration drives the anions from cathode to anode. The carbonate diffusion counteracts the migration because the production of hydroxide at the cathode results in a concentration gradient from the anode, where carbonate concentration is still high in the direction of the cathode, where carbonates have already been replaced by hydroxides. This process is called back-diffusion and is an important factor influencing the decarbonation dynamics of AEMs.

The observation of carbonate back-diffusion is consistent with literature results [20,28]. However diffusion has a lower relative contribution than in [28] because the diffusion length is much larger for the transport in the in-plane direction (16 mm) than for the transport in the through-plane direction in an AEMFC (0.059 mm).

In Fig. 4 b), the mechanisms of CO_2 release during the decarbonation process are displayed. The rates of CO_2 release from the electrochemical decarbonation at the anode, r_{a2} and r_{a3}, and from the chemical decarbonation via the membrane surface, r_{c1}, are compared. Chemical decarbonation and evaporation of CO_2 during equilibration corresponds to the decrease in bicarbonate in Fig. 2c. Approximately 2 h after the current has been switched on, the rate of the chemical decarbonation reaction falls to a value near zero. This drop coincides with the drop of the bicarbonate concentration to almost zero (see Fig. 2 c), which shifts the equilibrium of reaction (1) so that practically no dissolved CO_2 is present or produced anymore in the membrane. Even though the contact area between the membrane and the nitrogen atmosphere of the test setup is large, the chemical reaction does not contribute significantly to the decarbonation rate and the decarbonation via the anode dominates the self-purging mechanism.

This explains why the decarbonation of the LDPE-BTMA membrane takes a relatively long time of 50 h at 0.1 mA. The current density is relatively small due to its large cross-sectional area of 6.5×10^{-3} cm^2, whereas its IEC of 2.4 mmol g^{-1} is the largest among the membranes tested in the experiments. With a negligible contribution from chemical

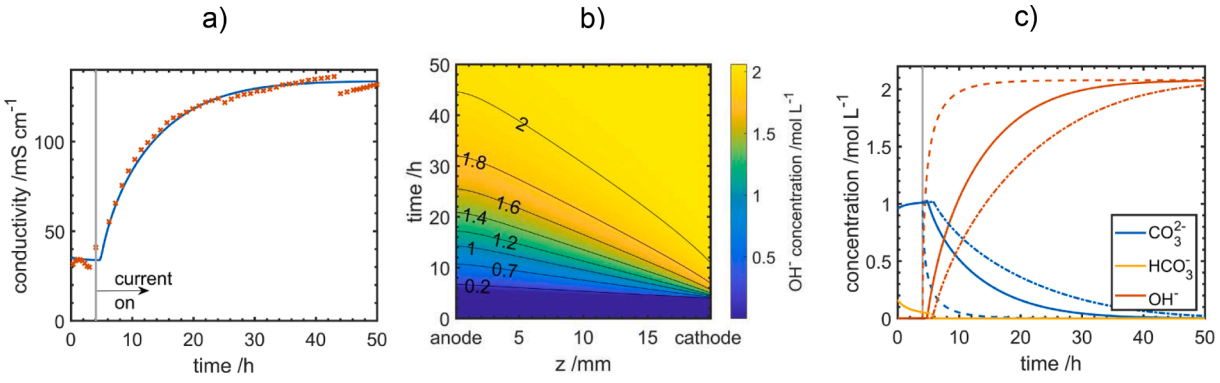

Fig. 2. Changes in the LDPE-BTMA membrane during the decarbonation process: a) experimental (red dots, adapted from [25]) and simulated (solid blue line) anion conductivity over time, b) hydroxide ion concentration over time and position in the membrane (black lines are isoconcentration lines), and c) anion concentrations over time at three different locations: dashed lines denote the concentrations at the cathode (z = 20 mm), dash-dotted lines at the anode (z = 0), and solid lines at the middle of the membrane (z = 10). The vertical grey lines in a) and c) denote the time when the current of 0.1 mA is switched on.

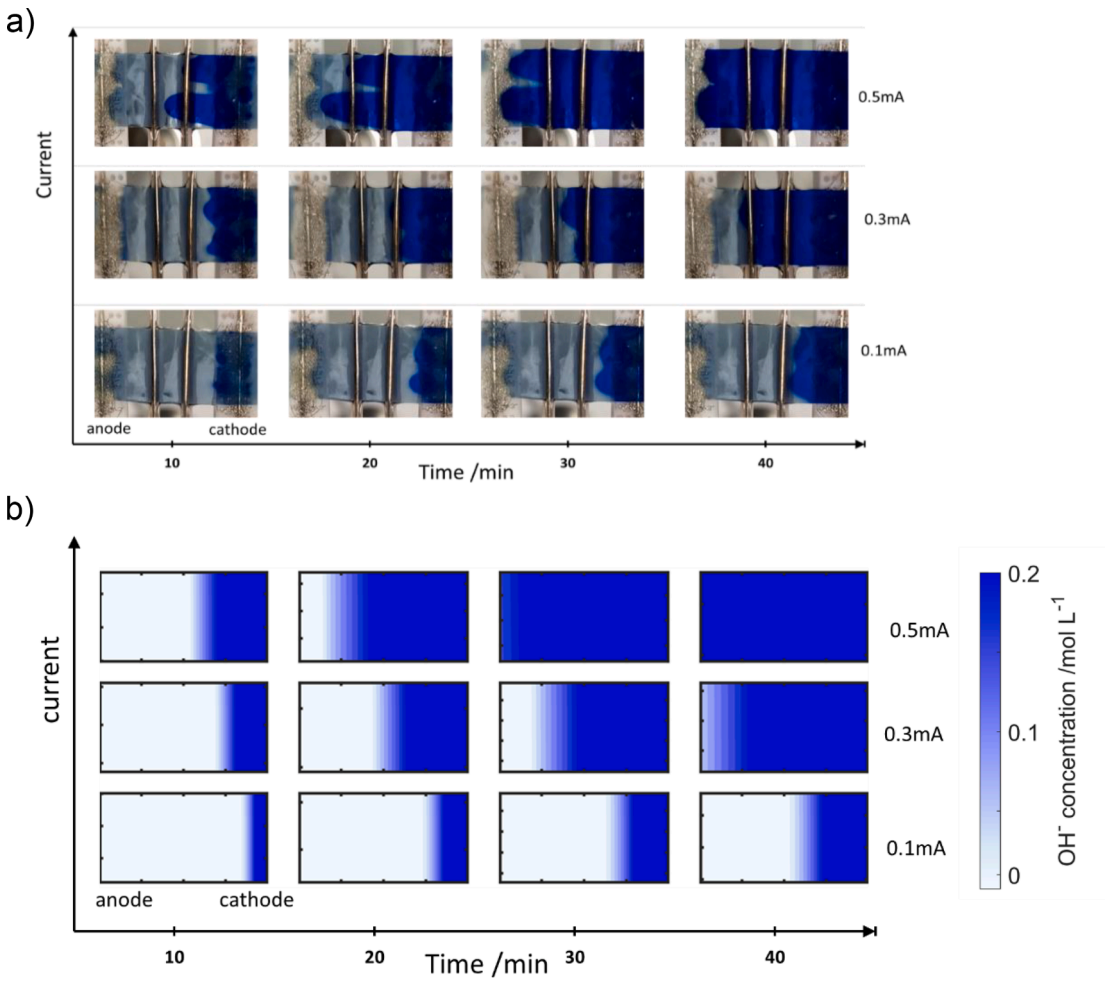

Fig. 3. A) visualization of the decarbonation process for an ldpe-btma membrane pretreated with 0.2 wt% thymolphthalein solution, for currents of 0.1, 0.3, and 0.5 mA. The current was applied at t = 0. The left electrode is the anode, the two middle electrodes are the sensing electrodes, and the right electrode is the cathode. The dark blue color represents higher hydroxide ion concentrations. b) Visualization of the simulation results for the experiments from a).

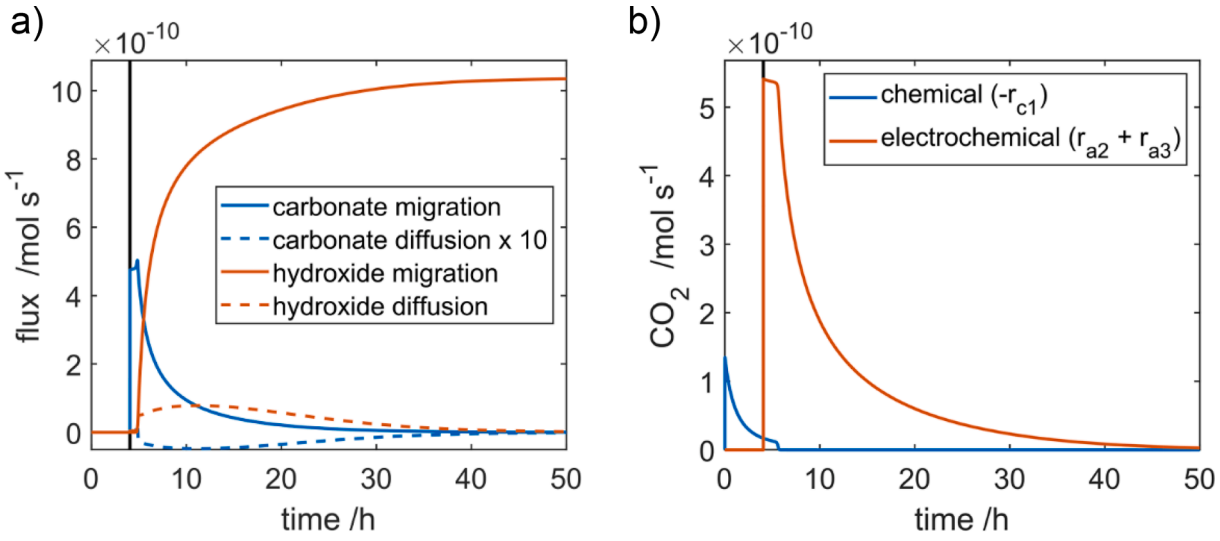

Fig. 4. a) Migrative and diffusive transport of OH^- and CO_3^{2-} over time in the middle of the LDPE-BTMA membrane. b) Rate of CO_2 release from the electrochemical decarbonation at the anode and the chemical decarbonation via the membrane surface. The vertical black line denotes the time when the current of 0.1 mA is switched on.

decarbonation via the membrane surface, a large amount of carbonate needs to be driven to the anode by a small current density which leads to a long decarbonation time.

Next, the decarbonation of the A201 membrane will be analyzed. The A201 membrane decarbonates comparatively quickly and the discussion will elucidate the differences between the A201 and the LDPE-BTMA membranes that can explain this behavior. The values of the ion diffusivities for the simulation ($D^{M}_{OH^-} = 2.9\ 10^{-8}\ m^2/s D^{M}_{CO_3^{2-}} = 3.1\ 10^{-9}\ m^2/s D^{M}_{HCO_3^-} = 6.2\ 10^{-9}\ m^2/s$) were identified by manually adjusting the diffusivities until an agreement of experiment and simulation was reached. The ion diffusivities of the A201 membrane are 1.5–2 times larger than those for the LDPE-BTMA membrane.

In Fig. 5 a), the simulated and experimental changes in conductivity over time are shown for the A201 membrane. The conductivity reaches a new stable value much faster. Accordingly, the plots of the ion concentrations in Fig. 5 b) and c) show that the A201 membrane is in its full OH^- form already after 20 h, compared to 50 h for the LDPE-BTMA membrane.

The reason for this behavior is the relatively high current density of the A201 membrane due to its ca. 50 % smaller cross-sectional area and its 30 % lower IEC compared to the LDPE-BTMA membrane (see Table 1). Exchanging a larger amount of carbonates (proportional to the IEC) at a smaller ionic current density is expected to take more time. The increase of decarbonation speed with a decreasing cross-sectional area, i.e., increasing current density, and the decreasing decarbonation speed with increasing IEC have been described before in experimental studies [25,31,42]. Thus, the simulations confirm the experimental results from the literature.

A further effect contributing to the faster decarbonation dynamics of the A201 membrane is illustrated by Fig. 6 a), where the rates of migrative and diffusive transport over time for OH^- and CO_3^{2-} are displayed. Transport by migration outweighs diffusive transport by an even larger factor than in the LDPE membrane. One hour after the current has been applied, migrative transport of OH^- is ca. 50 times larger than the diffusive transport (0.64 nmol s^{-1} vs 0.013 nmol s^{-1}), compared to around 11 times in the LDPE-BTMA membrane. Migrative transport of CO_3^{2-} is ca. 210 times larger than diffusive transport in absolute numbers (0.19 nmol s^{-1} vs − 0.0006 nmol s^{-1}). The minus sign indicates that diffusion acts in the opposite direction to migration. In the LDPE-BTMA membrane, diffusion also counteracts migration. Migration is faster than diffusion by a factor of ca. 320. Since the back-diffusion is a process that slows down the decarbonation dynamics by transporting carbonates from the anode back to the cathode, a lower relative contribution of diffusion causes faster dynamics.

The difference between A201 and LDPE-BTMA membrane partly results from the lower IEC of the A201 membrane because a lower IEC leads to smaller absolute concentration gradients and, thus, a lower driving force for diffusion. Also, the lower cross-sectional area reduces the rate of diffusion, whereas the total rate of migrative transport is fixed by the constant current of 0.1 mA.

The rates of the chemical and electrochemical decarbonation mechanism, which are shown in Fig. 6 b), show that the different decarbonation dynamics are not a result of changes in the decarbonation mechanism. Both the A201 and the LDPE-BTMA membranes are decarbonated almost exclusively via the anode reactions.

Up to this point, it can be concluded from the comparison of the two membranes that ion exchange capacity, current density, and carbonate back diffusion are critical factors that determine the dynamics of the decarbonation of AEMs. This brings valuable insights into the operation of AEMFCs under ambient air.

4.2. *Properties influencing AEM decarbonation dynamics*

Next, the model is used to investigate the influence of factors that are not easily accessible in an experiment. To facilitate the discussion, the dynamics of the decarbonation process were quantified by calculating a time constant τ from the simulated data assuming that the change in conductivity would follow an exponential equation of the following shape [25]:

$$\sigma(t) = \sigma_0 + \Delta\sigma\left(1 - \exp\left(-\frac{t}{\tau}\right)\right) \tag{42}$$

where σ(t) is the anion conductivity at time t, σ_0 is the initial conductivity, and Δσ is the difference between the final and the initial conductivity. The time constants reflect the differences in decarbonation speed that were discussed above: it is 9 h for the LDPE-BTMA membrane and 3.6 h for the A201 membrane.

Thus, the time constants provide some insights into the capability of the AEM to rapidly exchange its carbonates into hydroxide, even though lumping the dynamics and spatial distribution of the ion concentrations in the membrane into a single number is a substantial simplification.

In Fig. 7, the effect of selected membrane properties and parameters on the decarbonation time constant is shown for the example of the LDPE-BTMA membrane. Their effect is assessed by changing each model parameter value relative to the original values in Table 2 and 3.

In Fig. 7 a), the decarbonation time constant is depicted for variations of the normalized membrane thickness, IEC, current, and a simultaneous variation of IEC and current. Membrane thickness and IEC have an identical effect on the decarbonation time constant. Thus, their curves overlap completely. The time constant scales nearly linearly with both parameters because a larger value of either of the two parameters results in a larger total amount of carbonates that need to be purged out of the membrane. The fact that a thicker membrane poses a larger mass transfer resistance for transport from the inner membrane domains to the surface does not play a role since decarbonation via the membrane

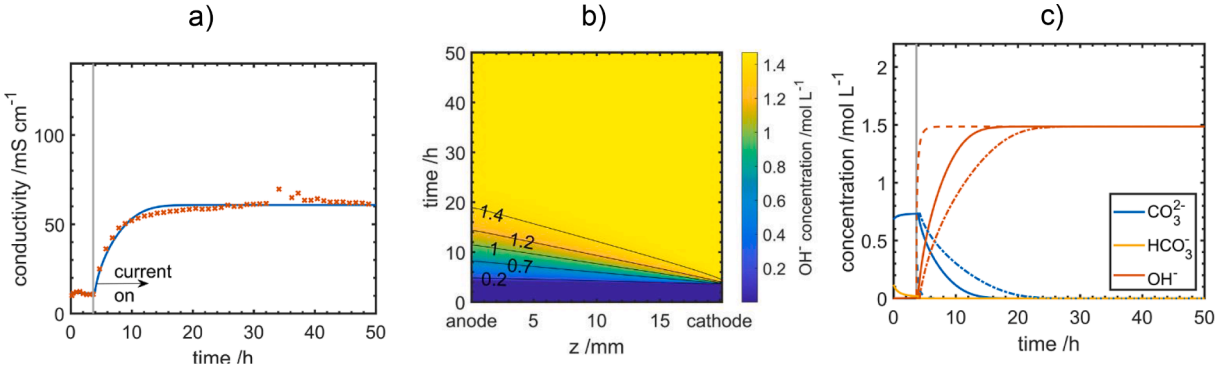

Fig. 5. a) Conductivity over time, b) Ion concentrations over time, and c) hydroxide ion concentration over time and position in the membrane during the decarbonation process for the A201 membrane. In b), dashed lines denote the concentrations at the cathode, dash-dotted lines the anode, and solid lines the middle of the membrane. The vertical grey lines in a) and b) denote the time when the current of 0.1 mA is switched on.

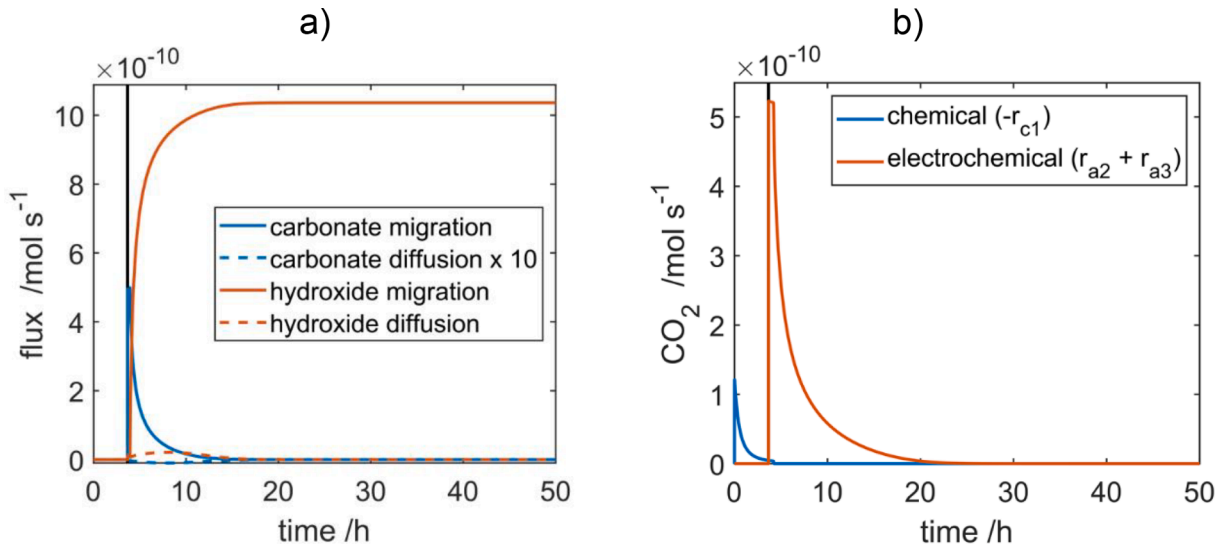

Fig. 6. a) Migrative and diffusive transport of OH^- and CO_3^{2-} over time in the middle of the A201 membrane. b) Rate of CO_2 release from the electrochemical decarbonation at the anode and the chemical decarbonation via the membrane surface. The vertical black line denotes the time when the current of 0.1 mA is switched on.

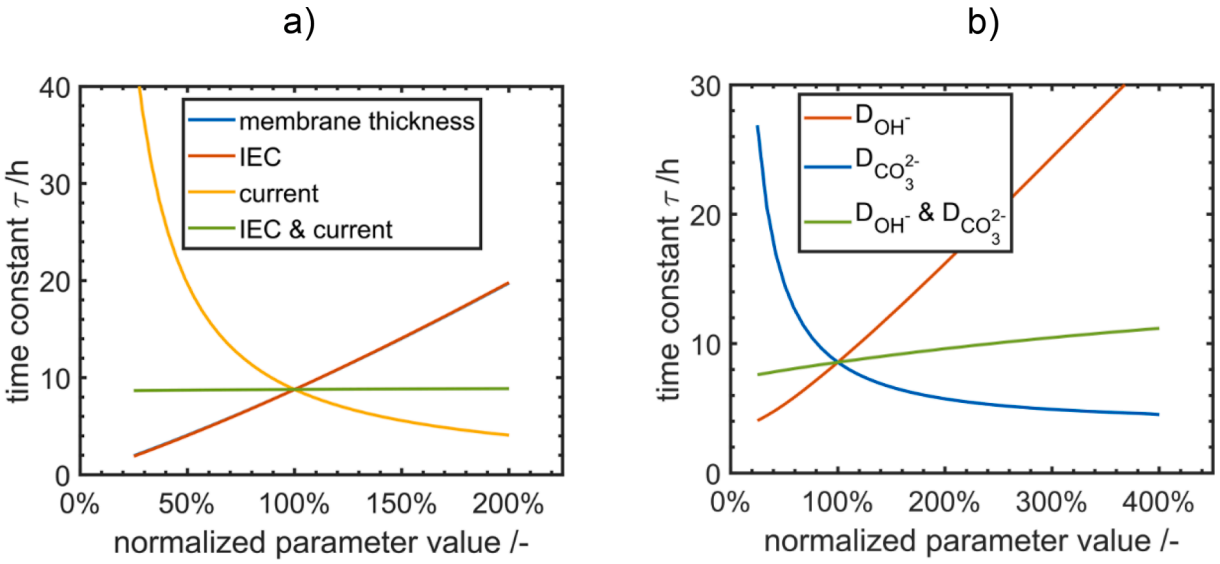

Fig. 7. Effect of various parameters on time constant τ of the decarbonation process for the LDPE-BTMA membrane. (a) effect of normalized membrane thickness, IEC and current, (b) effect of normalized diffusivities. The line for membrane thickness overlaps completely with the line for IEC (red). Values are normalized to the parameters given in Table 1 and 3; the reference value for the applied current is 0.1 mA.

surface is negligible (compare Fig. 4).

The time constant drops hyperbolically with the current. This positive effect of higher current (density) on the decarbonation of AEM and AEMFC is well documented in the literature [21,28,43] and results from the fact that the current is the main driving force for the decarbonation. When current and IEC are changed in parallel, the time constant remains unchanged because the effects cancel out each other.

The data in Fig. 7 a) indicates that AEMFC containing a thicker AEM or an AEM with a higher IEC would require a longer startup time or a higher current density to purge out carbonates that may have accumulated when the cell was not operating.

In Fig. 7 b), the decarbonation time constant is plotted over the normalized ion diffusivities. While it is not possible to synthesize membranes with specifically tailored diffusivities of individual ions, the conductivity ratio between AEM in hydroxide and carbonate form ranges between 4 and 8 [25], suggesting that the ratio of ion diffusivities of carbonate and bicarbonate is not constant in all materials. Furthermore, there is evidence that hydroxide diffusivities in AEM do not change monotonically with temperature, which implies that the ratio of hydroxide and carbonate conductivity would be a function of temperature [44]. Thus, the individual variation of the diffusivities can help interpret membrane characteristics and predict decarbonation time constants of future membranes.

The time constant decreases hyperbolically with increasing carbonate diffusivity (blue curve in Fig. 7 a)) and increases linearly with hydroxide diffusivity (red curve in Fig. 7 a)). The reason for this behavior is the dominant ion transport by migration. Because of the constant external current, the total ion current flowing through the membrane is constant. Inside the membrane, all ions are subject to the same driving force, i.e. potential gradient (see eq. (10)). The relative contributions of carbonates and hydroxides to the ionic current thus only depend on their relative contributions to the total membrane conductivity. The ionic

Table 3
Ion diffusivities and decarbonation time constants of alkaline exchange membranes.

Membrane	$D^{M}_{OH^-}$ (m^2/s)	$D^{M}_{HCO3^-}$ (m^2/s)	$D^{M}_{CO3^{2-}}$ (m^2/s)	coefficient of determination, R^2,	Simulated time constant τ (h) for the experiment's membrane geometry	Simulated time constant τ (h) for $w^M = 1$ cm and $d^M = 50$ μm
	*10^8	*10^8	*10^9			
A201	2.6	1.2	6.1	0.981	3.6	5.5
FAA-3	4.4	1.3	6.3	0.969	3.8	7.9
Sustanion RT	1.9	1.1	5.7	0.990	9.0	4.0
Sustanion 60	3.0	2.1	10.6	0.981	6.6	3.1
ETFE-TMA	2.2	0.8	4.1	0.987	6.5	7.8
AT-1	3.5	1.4	6.9	0.964	14.0	9.6
PF	7.2	2.7	13.4	0.935	4.8	4.4
LDPE-BTMA	1.4	0.8	4.1	0.993	9.0	6.7
ETFE-TMA, 0.5 mA	2.4	4.6	2.3	0.969	1.5	1.4
PAPip	2.9	1.0	5.0	0.994	11.7	8.8
QPAF-4(TM)	7.2	3.6	17.8	0.932	1.9	3.5

Note: The values of the diffusivity coefficients used in this work deviate from those reported in [25] because in [25] the Nernst-Einstein relation ($\sigma_{ion} = c^{M}_{ion} D^{eff}_{ion} z_{ion}{}^2 F^2 R^{-1} T^{-1}$) is used to obtain effective diffusivities from conductivity values instead of eq. (11).

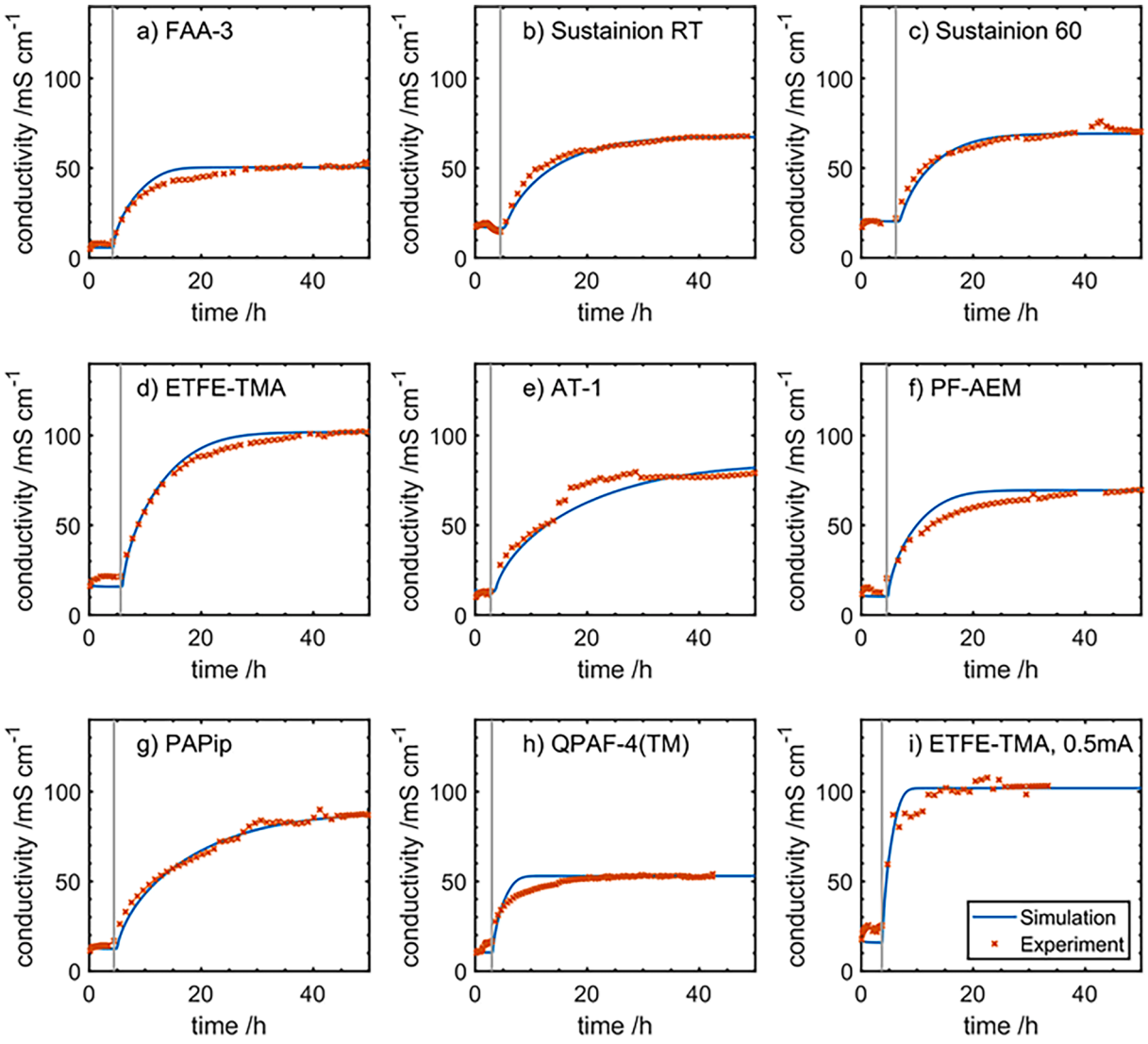

Fig. 8. Experimentally observed (symbols) and simulated (line) changes in anion conductivity of commercial and research AEMs before and after applying 0.1 mA direct current. Conductivity was measured at 95 % RH and 40 °C. AEM types: a), FAA-3b) Sustainion RT, c) Sustainion 60, d) ETFE-TMA, e) AT-1, f) PF, g) LDPE-BTMA, h) PAPip, i) QPAF-4 AEMs. j) shows contains results for an ETFE-TMA membrane when applying 0.5 mA current. The vertical grey line denotes the time when the current is switched on. The experimental data is from [25].

conductivity of each ion is directly proportional to its diffusivity (see eq. (12)). If hydroxide and carbonate conductivity are identical at a specific location in the membrane, identical migration fluxes towards the anode result. When the hydroxide diffusivity, and thus conductivity, increases, hydroxide transport by migration is increased and carbonate transport is decreased, resulting in an increase in the decarbonation time constant. Thus, the ratio of the diffusivities has a larger influence on the decarbonation time constant than the absolute diffusivities.

However, the effect of the absolute values of the diffusivities is not zero. The green curve in Fig. 7 b) shows the effect of increasing or decreasing both diffusivities in parallel. The curve is much flatter than the other two curves. The reason for this is the fact that the transport by migration is unaffected when both hydroxide and carbonate diffusivity increase by the same factor because their relative contribution to the ionic current does not change. However, the back diffusion of carbonates from the anode, which is counteracting the migration, becomes more important when the absolute diffusivity is increased. These results suggest that – contrary to what one might expect – higher hydroxide diffusivities come at the price of longer decarbonation times of AEM.

4.3. Model generalization to other AEM materials and current densities

The decarbonation dynamics of eight further AEM were simulated and compared to experimental decarbonation data from [25] to assess if the model can be used to describe a broad set of membranes with different properties.

Table 3 displays the identified ion diffusivities for the considered membranes as well as their time constants. All diffusivities were adjusted manually to obtain an agreement between the experiment and the simulation. Based on the observation that the ionic conductivity of most membranes is nearly identical in carbonate and bicarbonate form [45], the bicarbonate diffusivity coefficients were always set twice as large as the carbonate diffusivity coefficients.

The ratio between the diffusivity coefficients of hydroxide and bicarbonate and carbonate ions, $D^{M}_{OH^-}$ / $D^{M}_{HCO_3^-}$ and $D^{M}_{OH^-}/D^{M}_{CO_3^{2-}}$, of most of the AEMs are in the range of 1.5–3 and 3–7, which is consistent with recent self-diffusion coefficients of hydroxide and (bi)carbonate ions measured using ^{1}H- and ^{13}C-pulsed field gradient nuclear magnetic resonance [46]. The high diffusivity coefficients of both QPAF-4(TM) and PF can probably be attributed to the hydrophobic character of the fluorinated-based chemistries of those AEMs.

The coefficient of determination, R^2, between experimental and simulated conductivity is included in Table 3 to provide a simple measure for the quality of the fit. The values are all larger than 90 % and indicate that model output and experimental data agree well.

As can be seen in Fig. 8 a) to h), the dynamics of the decarbonation process are captured quite accurately for the different membrane materials. Some deviations between the experiment and simulation occur for the PF-AEM membrane and the QPAF-4 membrane. The reason could not be identified unambiguously. However, the membrane conductivity in carbonated state (before the current is applied) is not in a true steady-state. Thus, it seems likely that the deviations result from fluctuations in the experimental data rather than an inadequacy of the model. The fluctuations in the experiments may result from inhomogeneities of the research membranes with potentially less reproducible production process. Deviations between experiment and simulation may also result from the fact that membrane water uptake depends on the type of anion that is present in the membrane [47,48]. However, the effect has not been quantified for any of the membranes used in this study and could thus not be included in the model.

To further support the validity of the model predictions, conductivity data and simulation results for the decarbonation of an ETFE-TMA membrane with a five times higher external current of 0.5 mA are shown in Fig. 8 i). As expected, and as predicted by the model, the decarbonation proceeds much faster at the higher current. The good agreement between experimental data and simulation result demonstrates that the model also captures the effect of changing currents on the decarbonation process. The fluctuations in the experimental data in Fig. 8i) and a part of the deviation between the experiment and simulation may be caused by the higher current that induces a stronger oxygen and hydrogen formation at the anode and cathode.

It must be remarked that the agreement between the model and experimental data was obtained with a series of AEMs with very different characteristics in terms of water uptake, cross-sectional area, conductivity, and decarbonation dynamics (see Table 1 and 3). We conclude that the model accurately describes the decarbonation dynamics of AEMs. Further, it can be concluded that despite the different nature and properties of the membranes, all membranes can be described by the same model, including decarbonation kinetics, transport, and phase transfer. Their microscopic properties can be adequately lumped into macroscopic processes and parameters. Thus, once the diffusion parameters and the parameters from Table 1 of a given membrane are determined, the behavior can be predicted with the model. This holds not only for the setup modeled here but should also be applicable for AEMFC models.

Further, the trends on parameter dependency from Fig. 7 will be applicable, allowing the virtual design of optimal membranes for AEMFC decarbonization and dynamic behavior, e.g., during startup.

Finally, to identify which membrane material has the best decarbonation kinetics, the decarbonation time constant was simulated for a hypothetical set of membranes with identical dimensions of $w^M = 1$ cm and $d^M = 50$ µm. The Sustanion 60, QPAF-4(TM), and Sustanion RT membranes exhibit the shortest decarbonation time constants with 3.1, 3.5, and 4.0 h. This order differs strongly from the order that one would obtain from the membrane pieces of different geometrical dimensions used in the experiments and thus allow no direct comparison of the materials. It must be remarked here that the QPAF-4(TM) membrane exhibited deviations between the experiment and simulation.

This work provides new insights into the AEM decarbonation process, which are crucial for operating AEMFCs with ambient air or recently suggested applications of AEM-based electrochemical CO_2 capturing technologies [49].

5. Conclusions

In this work, we present an analysis of the *ex-situ* decarbonation process of AEM with an experimentally validated mechanistic model. The model can reproduce the experimentally observed decarbonation of ten different commercially available and researched AEMs, and thus, the presented findings may be extended to AEMs in general.

The ion concentration front that moves through the membrane during decarbonization was visualized by incorporating an indicator into the membrane. A very good agreement between this experiment and the simulation of the concentration front was observed, giving further credibility to the model.

It was found that decarbonation occurs almost exclusively via the anode and not via the membrane surface and ion transport is clearly dominated by migration. A parameter study showed that IEC and applied current have the largest effect on the decarbonation dynamics. Further, high hydroxide diffusivity values increase the decarbonation time constant, whereas high carbonate diffusivity values decrease the time constant. Interestingly, results indicate that high diffusivities of both carbonates and hydroxide result in a slower membrane decarbonation.

Finally, simulations were used to enable a fair comparison of the decarbonation dynamics between different membrane materials.

The successfully validated AEM model is suitable for integration into AEM fuel cells to study decarbonation and carbonation effects. The sequential process of external membrane parameterization and subsequent integration into fuel cell models is preferable to parameterization directly in AEM fuel cell models. The latter is difficult and error-prone,

because effects from the catalyst layers are present and because membrane humidity is difficult to control precisely. Further, the presented membrane parameterization and model was shown to be robust and work sucesfully for many AEMs, and thus promises a robust and reliable assessment of cell performance in presence of CO_2 and to design operational strategies, when integrating the parameterised membrane model into a cell model.

In the future, model accuracy may be further increased by including a dependency of membrane water uptake on the type of anion present in the membrane and by including equilibrium reactions between ions and cationic groups instead of using constant dissociation factors. Both measures depend on the availability of measured correlations.

Declaration of Competing Interest

The authors declare that they have no known competing financial interests or personal relationships that could have appeared to influence the work reported in this paper.

Data availability

Data will be made available on request.

Acknowledgment

This work was partially funded by the Nancy & Stephen Grand Technion Energy Program (GTEP); by the European Regional Development Fund [grant No. ZW6-85036745].

References

[1] N. Ralbag, M. Mann-Lahav, E.S. Davydova, U. Ash, R. Galed, M. Handl, R. Hiesgen, E. Magliocca, W. Mustain, J. He, P. Cong, A.M. Beale, G.S. Grader, D. Avnir, D. R. Dekel, Composite Materials with Combined Electronic and Ionic Properties, Matter. 1 (2019) 959–975, https://doi.org/10.1016/j.matt.2019.04.007.

[2] M. Bellini, M.V. Pagliaro, A. Lenarda, P. Fornasiero, M. Marelli, C. Evangelisti, M. Innocenti, Q. Jia, S. Mukerjee, J. Jankovic, L. Wang, J.R. Varcoe, C. B. Krishnamurthy, I. Grinberg, E. Davydova, D.R. Dekel, H.A. Miller, F. Vizza, Palladium-Ceria Catalysts with Enhanced Alkaline Hydrogen Oxidation Activity for Anion Exchange Membrane Fuel Cells, ACS Appl. Energy Mater. 2 (2019) 4999–5008, https://doi.org/10.1021/acsaem.9b00657.

[3] H. Yu, E.S. Davydova, U. Ash, H.A. Miller, L. Bonville, D.R. Dekel, R. Maric, Palladium-ceria nanocatalyst for hydrogen oxidation in alkaline media: Optimization of the Pd–CeO2 interface, Nano Energy. 57 (2019) 820–826, https://doi.org/10.1016/j.nanoen.2018.12.098.

[4] S. Lu, J. Pan, A. Huang, L. Zhuang, J. Lu, Alkaline polymer electrolyte fuel cells completely free from noble metal catalysts, Proc. Natl. Acad. Sci. 105 (2008) 20611–20614, https://doi.org/10.1073/pnas.0810041106.

[5] V. Men Truong, J. Richard Tolchard, J. Svendby, M. Manikandan, H.A. Miller, S. Sunde, H. Yang, D.R. Dekel, A. Oyarce Barnett, Platinum and Platinum Group Metal-Free Catalysts for Anion Exchange Membrane Fuel Cells, Energies. 13 (2020) 582, https://doi.org/10.3390/en13030582.

[6] J. Biemolt, J.C. Douglin, R.K. Singh, E.S. Davydova, N. Yan, G. Rothenberg, D. R. Dekel, An Anion-Exchange Membrane Fuel Cell Containing Only Abundant and Affordable Materials, Energy Technol. 9 (2021) 2000909, https://doi.org/10.1002/ente.202000909.

[7] Q. Hu, G. Li, J. Pan, L. Tan, J. Lu, L. Zhuang, Alkaline polymer electrolyte fuel cell with Ni-based anode and Co-based cathode, Int. J. Hydrogen Energy. 38 (2013) 16264–16268, https://doi.org/10.1016/j.ijhydene.2013.09.125.

[8] S. Gu, W. Sheng, R. Cai, S.M. Alia, S. Song, K.O. Jensen, Y. Yan, An efficient Ag–ionomer interface for hydroxide exchange membrane fuel cells, Chem. Commun. 49 (2013) 131–133, https://doi.org/10.1039/C2CC34862D.

[9] D.R. Dekel, Alkaline Membrane Fuel Cell (AMFC) Materials and System Improvement - State-of-the-Art, ECS Trans. 50 (2013) 2051–2052, https://doi.org/10.1149/05002.2051ecst.

[10] D.R. Dekel, Review of cell performance in anion exchange membrane fuel cells, J. Power Sources. 375 (2018) 158–169, https://doi.org/10.1016/j.jpowsour.2017.07.117.

[11] M. Ahmad, M. Yousaf, S. Wang, W. Cai, L. Sang, Z. Li, Z.-P. Zhao, Development of rapid CO2 utilizing microbial ecosystem onto the novel & porous FPUF@nZVI@TAC@ASP hybrid for green coal desulphurization, Chem. Eng. J. 433 (2022), 134361, https://doi.org/10.1016/j.cej.2021.134361.

[12] N. Ziv, W.E. Mustain, D.R. Dekel, The Effect of Ambient Carbon Dioxide on Anion-Exchange Membrane Fuel Cells, ChemSusChem. 11 (2018) 1136–1150, https://doi.org/10.1002/cssc.201702330.

[13] A.G. Divekar, A.M. Park, Z.R. Owczarczyk, S. Seifert, B.S. Pivovar, A.M. Herring, A Study of Carbonate Formation Kinetics and Morphological Effects Observed on OH - Form of Pfaem When Exposed to Air Containing CO 2, ECS Trans. 80 (2017) 1005–1011, https://doi.org/10.1149/08008.1005ecst.

[14] H. Yanagi, K. Fukuta, Anion Exchange Membrane and Ionomer for Alkaline Membrane Fuel Cells (AMFCs), ECS Trans. 16 (2008) 257–262, https://doi.org/10.1149/1.2981860.

[15] D. Schröder, N.N. Sinai Borker, M. König, U. Krewer, Performance of zinc air batteries with added K_2CO_3 in the alkaline electrolyte, J. Appl. Electrochem. 45 (2015) 427–437, https://doi.org/10.1007/s10800-015-0817-0.

[16] R. Vedarajan, R. Balaji, K. Ramya, Anion exchange membrane fuel cell: New insights and advancements, WIREs Energy Environ. (2022) 1–29. 10.1002/wene.466.

[17] D. Schröder, U. Krewer, Model based quantification of air-composition impact on secondary zinc air batteries, Electrochim. Acta. 117 (2014) 541–553, https://doi.org/10.1016/j.electacta.2013.11.116.

[18] T. Haisch, F. Kubannek, D. Chen, Y.J. Tong, U. Krewer, Origin of the Drastic Current Decay during Potentiostatic Alkaline Methanol Oxidation, ACS Appl. Mater. Interfaces. 12 (2020) 43535–43542, https://doi.org/10.1021/acsami.0c06547.

[19] M. Inaba, Y. Matsui, M. Saito, A. Tasaka, K. Fukuta, S. Watanabe, H. Yanagi, Effects of Carbon Dioxide on the Performance of Anion-Exchange Membrane Fuel Cells, Electrochemistry. 79 (2011) 322–325, https://doi.org/10.5796/electrochemistry.79.322.

[20] M.R. Gerhardt, L.M. Pant, A.Z. Weber, Along-the-Channel Impacts of Water Management and Carbon-Dioxide Contamination in Hydroxide-Exchange-Membrane Fuel Cells: A Modeling Study, J. Electrochem. Soc. 166 (2019) F3180–F3192. 10.1149/2.0171907jes.

[21] Y. Zheng, T.J. Omasta, X. Peng, L. Wang, J.R. Varcoe, B.S. Pivovar, W.E. Mustain, Quantifying and elucidating the effect of CO 2 on the thermodynamics, kinetics and charge transport of AEMFCs, Energy Environ. Sci. 12 (2019) 2806–2819, https://doi.org/10.1039/C9EE01334B.

[22] J.A. Vega, C. Chartier, W.E. Mustain, Effect of hydroxide and carbonate alkaline media on anion exchange membranes, J. Power Sources. 195 (2010) 7176–7180, https://doi.org/10.1016/j.jpowsour.2010.05.030.

[23] S. Srebnik, S. Pusara, D.R. Dekel, Effect of Carbonate Anions on Quaternary Ammonium-Hydroxide Interaction, J. Phys. Chem. C. 123 (2019) 15956–15962, https://doi.org/10.1021/acs.jpcc.9b03131.

[24] Y. Zheng, G. Huang, L. Wang, J.R. Varcoe, P.A. Kohl, W.E. Mustain, Effect of reacting gas flowrates and hydration on the carbonation of anion exchange membrane fuel cells in the presence of CO2, J. Power Sources. 467 (2020), 228350, https://doi.org/10.1016/j.jpowsour.2020.228350.

[25] A. Zhegur-Khais, F. Kubannek, U. Krewer, D.R. Dekel, Measuring the true hydroxide conductivity of anion exchange membranes, J. Memb. Sci. 612 (2020), 118461, https://doi.org/10.1016/j.memsci.2020.118461.

[26] N. Ziv, D.R. Dekel, A practical method for measuring the true hydroxide conductivity of anion exchange membranes, Electrochem. Commun. 88 (2018) 109–113, https://doi.org/10.1016/j.elecom.2018.01.021.

[27] C. Simari, E. Lufrano, M.H.U. Rehman, A. Zhegur-Khais, S. Haj-Bsoul, D.R. Dekel, I. Nicotera, Effect of LDH platelets on the transport properties and carbonation of anion exchange membranes, Electrochim. Acta. 403 (2022), 139713, https://doi.org/10.1016/j.electacta.2021.139713.

[28] U. Krewer, C. Weinzierl, N. Ziv, D.R. Dekel, Impact of carbonation processes in anion exchange membrane fuel cells, Electrochim. Acta. 263 (2018) 433–446, https://doi.org/10.1016/j.electacta.2017.12.093.

[29] T.D. Myles, K.N. Grew, A.A. Peracchio, W.K.S. Chiu, Transient ion exchange of anion exchange membranes exposed to carbon dioxide, J. Power Sources. 296 (2015) 225–236, https://doi.org/10.1016/j.jpowsour.2015.07.044.

[30] J.A. Wrubel, A.A. Peracchio, B.N. Cassenti, K.N. Grew, W.K.S. Chiu, Anion Exchange Membrane Fuel Cell Performance in the Presence of Carbon Dioxide: An Investigation into the Self-Purging Mechanism, J. Electrochem. Soc. 166 (2019) F810–F820. 10.1149/2.0801912jes.

[31] X. Cao, D. Novitski, S. Holdcroft, Visualization of Hydroxide Ion Formation upon Electrolytic Water Splitting in an Anion Exchange Membrane, ACS Mater. Lett. 1 (2019) 362–366, https://doi.org/10.1021/acsmaterialslett.9b00195.

[32] J. Ponce-Gonzalez, D.K. Whelligan, L. Wang, R. SOUALHI, Y. Wang, Y. Peng, H. Peng, D.C. Apperley, H.N. Sarode, T.P. Pandey, A.G. Divekar, S. Seifert, A. Herring, L. Zhuang, J.R. Varcoe,, High performance aliphatic-heterocyclic benzyl-quaternary ammonium radiation-grafted anion-exchange membranes, Energy Environ. Sci. (2016), https://doi.org/10.1039/C6EE01958G.

[33] L. Wang, M. Bellini, H.A. Miller, J.R. Varcoe, A high conductivity ultrathin anion-exchange membrane with 500+ h alkali stability for use in alkaline membrane fuel cells that can achieve 2 W cm-2 at 80 °c, J. Mater. Chem. A. 6 (2018) 15404–15412, https://doi.org/10.1039/c8ta04783a.

[34] A.M. Park, Z.R. Owczarczyk, L.E. Garner, A.C. Yang-Neyerlin, H. Long, C. M. Antunes, M.R. Sturgeon, M.J. Lindell, S.J. Hamrock, M. Yandrasits, B.S. Pivovar, Synthesis and Characterization of Perfluorinated Anion Exchange Membranes, ECS Trans. 80 (2017) 957–966, https://doi.org/10.1149/08008.0957ecst.

[35] J.S. Olsson, T.H. Pham, P. Jannasch, Tuning poly(arylene piperidinium) anion-exchange membranes by copolymerization, partial quaternization and

crosslinking, J. Memb. Sci. 578 (2019) 183–195, https://doi.org/10.1016/j.memsci.2019.01.036.
[36] H. Ono, T. Kimura, A. Takano, K. Asazawa, J. Miyake, J. Inukai, K. Miyatake, Robust anion conductive polymers containing perfluoroalkylene and pendant ammonium groups for high performance fuel cells, J. Mater. Chem. A. 5 (2017) 24804–24812, https://doi.org/10.1039/c7ta09409d.
[37] J.C. Douglin, J.R. Varcoe, D.R. Dekel, A high-temperature anion-exchange membrane fuel cell, J. Power Sources Adv. 5 (2020), 100023, https://doi.org/10.1016/j.powera.2020.100023.
[38] J. Yan, M.A. Hickner, Anion Exchange Membranes by Bromination of Benzylmethyl-Containing Poly(sulfone)s, Macromolecules. 43 (2010) 2349–2356, https://doi.org/10.1021/ma902430y.
[39] T.P. Pandey, A.M. Maes, H.N. Sarode, B.D. Peters, S. Lavina, K. Vezzù, Y. Yang, S. D. Poynton, J.R. Varcoe, S. Seifert, M.W. Liberatore, V. Di Noto, A.M. Herring, Interplay between water uptake, ion interactions, and conductivity in an e-beam grafted poly(ethylene-co-tetrafluoroethylene) anion exchange membrane, Phys. Chem. Chem. Phys. 17 (2015) 4367–4378, https://doi.org/10.1039/C4CP05755D.
[40] K.N. Grew, X. Ren, D. Chu, Effects of Temperature and Carbon Dioxide on Anion Exchange Membrane Conductivity, Electrochem. Solid-State Lett. 14 (2011) B127, https://doi.org/10.1149/2.011112esl.
[41] W.A. Cole, W.A. Wakeham, The Viscosity of Nitrogen, Oxygen, and Their Binary Mixtures in the Limit of Zero Density, J. Phys. Chem. Ref. Data. 14 (1985) 209–226, https://doi.org/10.1063/1.555748.
[42] S. Haj-Bsoul, J.R. Varcoe, D.R. Dekel, Measuring the alkaline stability of anion-exchange membranes, J. Electroanal. Chem. 908 (2022), 116112, https://doi.org/10.1016/j.jelechem.2022.116112.
[43] Y. Matsui, M. Saito, A. Tasaka, M. Inaba, Influence of Carbon Dioxide on the Performance of Anion-Exchange Membrane, Fuel Cells 25 (2010) 105–110, https://doi.org/10.1149/1.3315177.
[44] T. Zelovich, L. Vogt-Maranto, C. Simari, I. Nicotera, M.A. Hickner, S.J. Paddison, C. Bae, D.R. Dekel, M.E. Tuckerman, Non-Monotonic Temperature Dependence of Hydroxide Ion Diffusion in Anion Exchange Membranes, Chem. Mater. 34 (2022) 2133–2145, https://doi.org/10.1021/acs.chemmater.1c03594.
[45] N. Ziv, A.N. Mondal, T. Weissbach, S. Holdcroft, D.R. Dekel, Effect of CO2 on the properties of anion exchange membranes for fuel cell applications, J. Memb. Sci. 586 (2019) 140–150, https://doi.org/10.1016/j.memsci.2019.05.053.
[46] T. Zelovich, C. Simari, I. Nicotera, D.R. Dekel, M.E. Tuckerman, The impact of carbonation on hydroxide diffusion in nano-confined anion exchange membranes, Submitt. to J. Mater. Chem. A. (2022).
[47] J. Peng, A.L. Roy, S.G. Greenbaum, T.A. Zawodzinski, Effect of CO2 absorption on ion and water mobility in an anion exchange membrane, J. Power Sources. 380 (2018) 64–75, https://doi.org/10.1016/j.jpowsour.2018.01.071.
[48] Y. Zheng, L.N. Irizarry Colón, N. Ul Hassan, E.R. Williams, M. Stefik, J. M. LaManna, D.S. Hussey, W.E. Mustain, Effect of Membrane Properties on the Carbonation of Anion Exchange Membrane Fuel Cells, Membranes (Basel) 11 (2021) 102, https://doi.org/10.3390/membranes11020102.
[49] Y. Zheng, G. Huang, M. Mandal, J.R. Varcoe, P.A. Kohl, W.E. Mustain, Editors' Choice—Power-Generating Electrochemical CO 2 Scrubbing from Air Enabling Practical AEMFC Application, J. Electrochem. Soc. 168 (2021), 024504, https://doi.org/10.1149/1945-7111/abe08a.